communications materials

ARTICLE

Check for updates

https://doi.org/10.1038/s43246-023-00428-6 OPEN

Enhanced luminescence efficiency in Eu-doped GaN superlattice structures revealed by terahertz emission spectroscopy

Fumikazu Murakami[1], Atsushi Takeo[2], Brandon Mitchell[2,3,4], Volkmar Dierolf[4], Yasufumi Fujiwara[2] & Masayoshi Tonouchi[1✉]

Eu-doped Gallium nitride (GaN) is a promising candidate for GaN-based red light-emitting diodes, which are needed for future micro-display technologies. Introducing a superlattice structure comprised of alternating undoped and Eu-doped GaN layers has been observed to lead to an order-of-magnitude increase in output power; however, the underlying mechanism remains unknown. Here, we explore the optical and electrical properties of these superlattice structures utilizing terahertz emission spectroscopy. We find that ~0.1% Eu doping reduces the bandgap of GaN by ~40 meV and increases the index of refraction by ~20%, which would result in potential barriers and carrier confinement within a superlattice structure. To confirm the presence of these potential barriers, we explored the temperature dependence of the terahertz emission, which was used to estimate the barrier potentials. The result revealed that even a dilutely doped superlattice structure induces significant confinement for carriers, enhancing carrier recombination within the Eu-doped regions. Such an enhancement would improve the external quantum efficiency in the Eu-doped devices. We argue that the benefits of the superlattice structure are not limited to Eu-doped GaN, which provides a roadmap for enhanced optoelectronic functionalities in all rare-earth-doped semiconductor systems.

[1] Institute of Laser Engineering, Osaka University, 2-6 Yamada-oka, Suita, Osaka 565-0871, Japan. [2] Graduate School of Engineering, Osaka University, 2-1 Yamada-oka, Suita, Osaka 565-0871, Japan. [3] Department of Physics and Engineering, West Chester University, 700 South High Street, West Chester, PA 19383, USA. [4] Department of Physics, Lehigh University, 27 Memorial Dr W, Bethlehem, PA 18015, USA. ✉email: tonouchi.masayoshi.ile@osaka-u.ac.jp

The ubiquity of light-emitting diodes (LEDs) in our everyday life is undeniable, and micro-LEDs are now being rapidly developed to usher in a new wave of display technologies. One obstacle to realizing these technologies is the lack of an efficient red LED based on GaN. Currently, most full-color LED displays are made by combining green and blue GaN-based LEDs with traditional red GaAs-based LEDs using the pick-and-place technique[1]. A long-standing issue with fabricating GaN-based red LEDs is the large Indium content required in the InGaN layers, which introduces strain and reduces efficiency due to the quantum-confined Stark effect and indium phase separation[2–6]. For micro-LEDs in general, InGaN faces two additional challenges associated with the reduction in device size: a sharp decrease in external quantum efficiency (EQE) due to leakage current at the device walls and significant blue shifts in peak emission wavelength due to band-filling effects[7]. The leakage current increases for smaller devices[8,9], due to the non-radiative recombination at the sidewalls of the micro-LED structures. Despite these challenges, blue and green GaN-based micro-LEDs with EQEs of 13% and 25%, respectively, for an active area of 1 μm^2 were reported[10,11]. However, the EQE of red micro-LED remains below 5% for active regions smaller than 100 μm^2[11–14]. Once these challenges are overcome, micro-LEDs will facilitate the development of innovative technologies such as augmented reality and transparent displays[15].

Eu-doped GaN-based LEDs represent an alternative path towards full-color monolithic displays and offer favorable properties over InGaN LEDs, especially for micro-LED applications. Figure 1 shows monolithically grown blue (InGaN) and red (Eu-doped GaN) micro-LEDs with a 20 μm width. For Eu-doped GaN LEDs, the red emission at ~620 nm originates from intra-*4f* transitions within the Eu^{3+} ions[16]. As with all rare earth (RE) ions, Eu^{3+} ions exhibit sharp and spectrally stable emission regardless of the host system or excitation conditions. Additionally, Eu-doped materials have been shown to be less influenced by non-radiative sidewall defects due to their short carrier diffusion lengths[17,18]. They have also been used to realize monolithically stacked full-color LEDs on a single chip[19]. These properties make Eu-doped GaN a promising candidate for micro-LED applications.

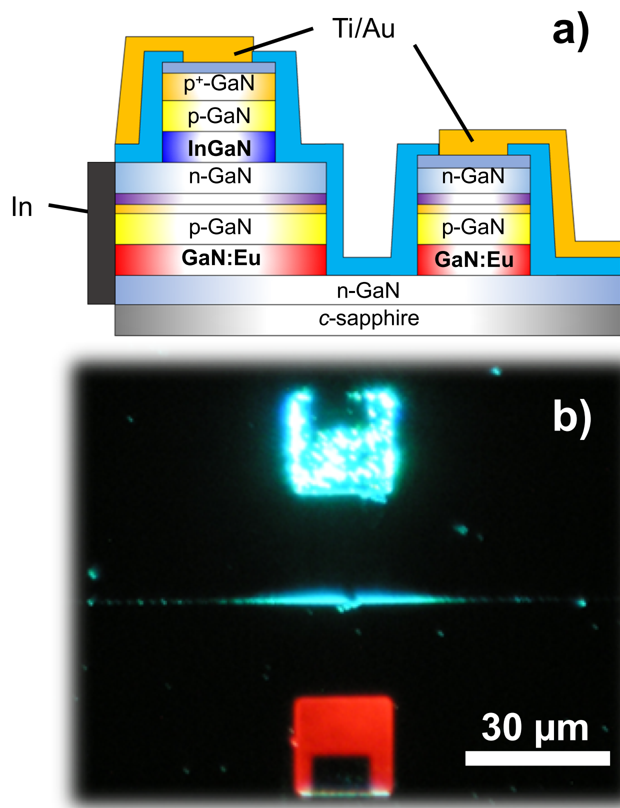

Fig. 1 Monolithically grown two-color micro-LED. a Schematic for monolithically grown blue (InGaN) and red (Eu-doped GaN) micro-LEDs. **b** Prototype of a monolithically grown two-color micro-LED array with 20 μm wide pixels.

The output power of Eu-doped GaN devices now exceeds 1.2 mW with EQEs as high as 9.2%. This was achieved using a superlattice structure consisting of alternating GaN and Eu-doped GaN layers, resulting in a 25-fold increase[16,19]. While this performance far exceeds that of devices grown using single active layers of Eu-doped GaN, the exact origin of the increased output power and EQE remains unknown[16]. Using atomic force and transmission electron microscopy, it was shown that the size and density of threading dislocations were significantly reduced in superlattice samples, which would reduce leakage current and could partially explain the improved electrical properties of the superlattice structure[20]. In addition, these results also showed that the lattice expanded within the Eu-doped layers relative to the undoped layers. A similar enhancement in luminescence and device performance was reported for superlattice devices consisting of alternating Si/Er-Si layers, which also outperformed monolayer-based devices by over an order of magnitude, at 80 K[21–25]. In this case, the enhancement has simply been explained as an increase in the efficiency of the energy transfer between the host and the RE ions or the selective formation of highly efficient defect centers[26]. However, there may be a deeper underlying mechanism for this enhancement.

The origin of these enhancements may be related to reports in other RE-doped semiconductor systems used for different applications[24,27–34]. For example, the doping of RE ions, such as Eu, Nd, Er, Tb, and Sm into semiconductor nanoparticles such as TiO_2 and ZnO has been used for nearly two decades to modify the bandgap of the nanoparticles themselves, which makes the host materials more suitable for certain applications, such as photovoltaics[27,28,30,31]. Dopant concentrations typically exceed 2%; however, this behavior has also been observed for dilute dopant levels of ~0.5%. Since the optical band gap and index of refraction are related quantities[35], it is not surprising that several other groups have also reported an increase in the index of refraction due to dilute doping[25,36], which could be used to fabricate integrated waveguides for telecommunication applications[36,37]. However, there are no reports, to the best of our knowledge, on the simultaneous measurement of bandgap and index of refraction changes due to RE doping, or the use of superlattice structures to enhance optoelectronic properties of RE-based devices due to the carrier confinement and waveguiding that should result. To this end, probing the carrier behavior in the Eu-doped GaN superlattice structure is necessary to understand the device performance and further optimize these devices.

Here, we employed terahertz (THz) emission spectroscopy (TES) to study the dynamics of photoinduced carriers in the Eu-doped superlattice structures as compared to single-layer Eu-doped GaN samples. When photocarriers are excited in semiconductors by femtosecond (fs) optical pulses, they are accelerated by a built-in electric field. This acceleration generates THz radiation that reflects the carrier movement within the first few picoseconds after excitation. The waveforms and amplitudes can provide physical information on a wide range of device materials and structures, such as the semiquantitative estimation of semiconductor surface/interface potentials, in a non-contact and non-destructive manner[38–41]. This technique is particularly useful for

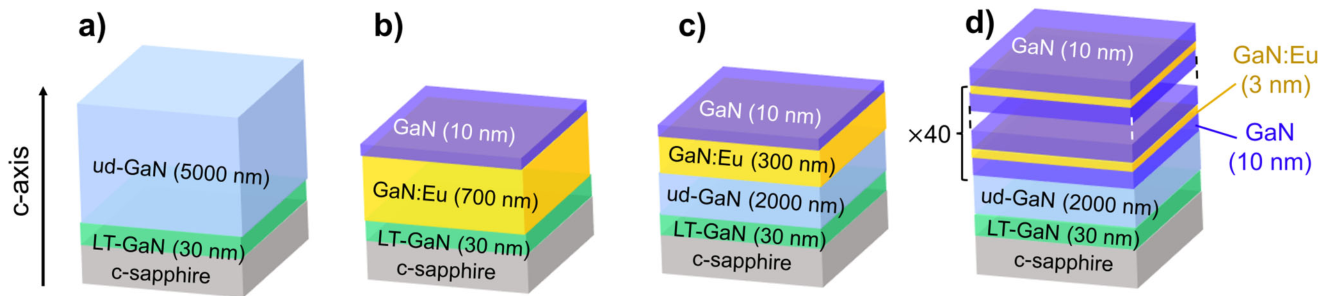

Fig. 2 Structures for the samples studied in this work. a ud-GaN, (**b**) GaN:Eu$_{TDS}$, (**c**) GaN:Eu$_{low,high}$, (**d**) superlattice. All structures were grown on the low-temperature-grown (LT)-GaN, which were grown on c-plain sapphire substrates.

wide bandgap semiconductor evaluation as it allows for the direct measurement of the material's bandgap[41,42]. In many cases, measuring the bandgap energy using room-temperature photoluminescence (PL) is difficult in semiconductors with a high concentration of impurities or dopants. However, TES solely results from excitation to the conduction band and is not influenced by impurity levels and provides a new platform to discuss the ultrafast photocarrier dynamics of wide bandgap semiconductors[43–47]. Thus, TES is an ideal tool to study the mechanism behind the enhanced properties of dilutely doped RE-based superlattice optoelectronic devices, and Eu-doped GaN serves as an example system for the utility of these properties.

Results

Bandgap reduction due to Eu doping. The structures of all samples used in this study are shown in Fig. 2. Measurements were taken on undoped GaN (Fig. 2a), a thick Eu-doped GaN sample (Fig. 2b), GaN doped with low and high Eu concentrations (Fig. 2c), and a superlattice structure consisting of 40 pairs of alternating Eu-doped GaN (3 nm) and GaN (10 nm) layers (Fig. 2d). These samples are labeled ud-GaN, GaN:Eu$_{TDS}$, GaN:Eu$_{low}$ and GaN:Eu$_{high}$, and superlattice, respectively.

The bandgap of a semiconductor material can be determined with meV precision by evaluating the excitation wavelength dependence of the emitted THz signal within 10 ps of excitation[43,48]. This behavior was used to determine the influence of dilute Eu doping on the bandgap of GaN. Figures 3a–c shows the time evolution of the THz emission obtained from the ud-GaN, GaN:Eu$_{low}$, and GaN:Eu$_{high}$ samples, where the THz signals are shown for different excitation wavelengths, at room temperature. Since the bandgap of ud-GaN is ~361 nm at room temperature[49,50], the THz signals should be strong for excitation wavelengths of <361 nm, for all samples. On the other hand, the THz signal was clearly visible even at 365 nm excitation for GaN:Eu$_{high}$. We have previously shown that polarity of the THz emission was dependent on the GaN conducting type. This indicates that the THz emission from the GaN surface is caused by the photocurrent in the surface electric field[41,47].

Figure 3d shows the peak amplitudes of the THz emission at ~10 ps as a function of excitation wavelength for all three samples. The black, blue, and red data points correspond to ud-GaN, GaN:Eu$_{low}$ and GaN:Eu$_{high}$, respectively. (See Supplementary Note 1 and Supplementary Fig. 1 for details on the superlattice structure measurements). Among these samples, GaN:Eu$_{low}$ exhibited the highest emission amplitude. This is attributed to changes in surface potential and carrier mobility due to the Eu doping. Here, the THz emission amplitude can be described by

$$|E_{\mathrm{THZ}}| \propto \mu E_{\mathrm{Max}} I_{\mathrm{p}} \propto \mu \frac{V_{\mathrm{D}}}{\lambda_{\mathrm{L}}} I_{\mathrm{p}}, \qquad (1)$$

where μ is the carrier mobility, I_p is the injection photon flux, V_D is the diffusion voltage, and λ_L is the penetration depth of excitation pulses[41,48]. Eu-doped GaN has shown a larger surface potential and smaller carrier mobility compared to ud-GaN[17,51]. These changes cancel each other in Eq. (1). Consequently, GaN:Eu$_{high}$ showed a similar amplitude to ud-GaN. However, in GaN:Eu$_{low}$, carrier mobility might be higher than that in GaN:Eu$_{high}$ due to a lower concentration of Eu doping. As a result, the emission from GaN:Eu$_{low}$ was larger than the others. To gain further insight, we need to obtain the doping concentration dependence of the penetration depth, surface potential, and carrier mobility accurately. However, these discussions are beyond the scope of the present study and are left for future work.

The THz emission by the optical rectification has shown to be not dominant in the emission from c-plane GaN bulk samples[41,47]. We also explored the influence of optical rectification on the emission from the superlattice sample as shown in Supplementary Fig. 2, which suggested the less/no nonlinear effect. Therefore, we can rule out the nonlinear effect as the THz emission mechanism in this work (See Supplementary Note 2 and Supplementary Fig. 2 for information about the THz emission property). This means that the THz emission is only generated when photocarriers are excited by photons with an energy larger than the bandgap of the material. Once the excitation energy falls below the bandgap, the THz emission amplitude will go to zero, and we can use this drop-off in amplitude to determine the bandgap energy. However, to extract the bandgap from the curves shown in Fig. 3d, we must take into account the spectral width of the fs excitation pulses, which have a broad wavelength profile due to the relationship between energy and time. To do this, we assume that the spectral profile of the fs pulses follows a hyperbolic secant distribution. Under this assumption, the THz emission amplitude E_{THz} can be described by,

$$|E_{\mathrm{THz}}| \propto \int_0^{(\lambda_{\mathrm{g}})} \mathrm{sech}^2(A(\lambda - \lambda_{\mathrm{p}}))d\lambda \qquad (2)$$

where A is a fitting parameter, λ_g is a wavelength corresponding to the bandgap energy, λ_p is a center wavelength of fs excitation pulses[41]. The solid curves in Fig. 3d are fits of the data using Eq. (2). From these fits, we obtained bandgap energies (and corresponding wavelengths) of 3.430 ± 0.003 eV (361.5 ± 0.3 nm), 3.419 ± 0.002 eV (362.7 ± 0.2 nm), and 3.393 ± 0.002 eV (365.5 ± 0.2 nm) for ud-GaN, GaN:Eu$_{low}$, and GaN:Eu$_{high}$, respectively (we showed the stability and validity of this measurement in Supplementary Note 3 and Supplementary Figs. 3–5). The determined bandgap energy of ud-GaN was consistent with previously reported values at room temperature[41,49,50], while the bandgap energy of the Eu-doped samples was found to decrease with increasing Eu concentration.

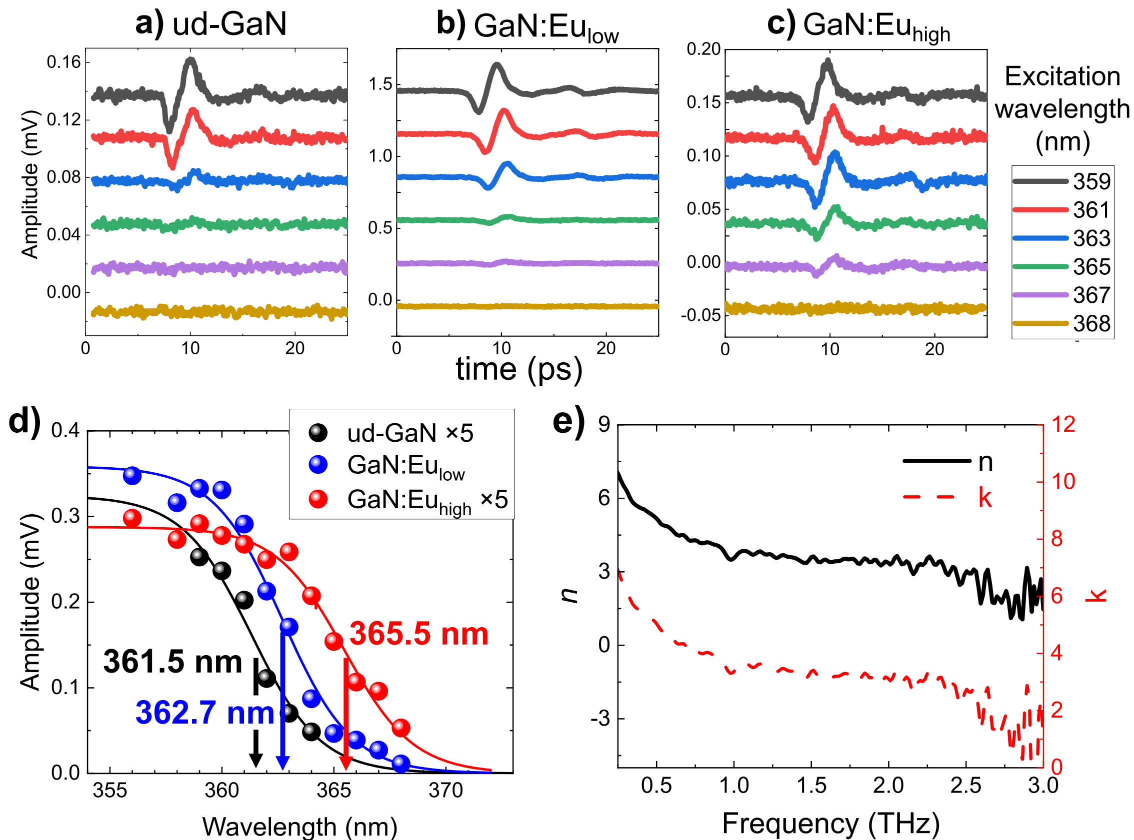

Fig. 3 THz emission and time-domain spectroscopy for bulk GaN samples. THz waveforms emitted from (**a**) ud-GaN, (**b**) GaN:Eu$_{low}$, and (**c**) GaN:Eu$_{high}$ with various excitation wavelengths at room temperature. Each color of the waveforms represents excitation at 359–368 nm. **d** Peak THz amplitudes at $t = 10$ ps of the waveforms shown in the (**a**–**c**) plotted as a function of excitation wavelengths. Black, blue, and red solid circles correspond to ud-GaN, GaN:Eu$_{low}$, and GaN:Eu$_{high}$, respectively. Data for ud-GaN and GaN:Eu$_{high}$ are enlarged by a factor of 5. Solid lines are fits to the THz amplitudes using Eq. (2). **e** Refractive index n (black solid line) and extinction coefficient k (red dashed line) in Eu-doped GaN for a range of THz frequencies as measured by THz time-domain spectroscopy.

The total bandgap difference between ud-GaN and GaN:Eu$_{high}$ was found to be ~37 meV.

In this calculation, the absorption difference under different excitation wavelengths was not considered because the difference is negligible within the energy range above the bandgap[52]. Although the absorption difference is larger in the wavelength range below the bandgap, the THz emission should be much smaller compared to the above bandgap excitation. In addition, we disregarded the influences of the interfaces between ud-GaN/low-temperature-grown(LT)-GaN or GaN:Eu/ud-GaN in this work. Since the fermi level in the n-type GaN materials is nearly independent on the carrier concentration[53,54], we expect the fermi level in the GaN:Eu to be almost the same as the ud-GaN (Carrier density in the GaN:Eu will be obtained in the later section). Consequently, it seems that no significant band bending was formed between these layers. In addition, the depletion layer thickness w can be described as

$$w = \sqrt{\frac{2\varepsilon_r \varepsilon_0 V_D}{e^2 N_D}}, \tag{3}$$

where ε_r is the dielectric constant of GaN ($\varepsilon_r = 9.5$[55]), ε_0 is the vacuum permittivity, e is the electron charge, and N_D is the donor concentration. Since obtaining the activated donor density is often challenging, we approximated it using the measured carrier density N. w at GaN:Eu surface was estimated to be ~0.53 µm using $V_D = 1.61$ eV[41,51], $N = 6 \times 10^{17}$ cm^{-3} (mentioned in the next section), and $\varepsilon_r = 9.5$[55]. Since this value is smaller than the thickness of the GaN:Eu layer, the GaN:Eu/ud-GaN interface should not influence the THz emission from the surface depletion layer. Additionally, the penetration depth for an excitation wavelength of 360 nm is ~0.8-1 µm in GaN[41]. This suggests that the excitation pulses could not reach the ud-GaN/LT-GaN interface. Therefore, it seems that the interfaces in GaN:Eu samples did not influence the optical properties and THz emissions in this work.

Index of refraction and extinction coefficient in Eu-doped GaN. Terahertz time-domain spectroscopy (THz-TDS) was used to obtain the refractive index (n), extinction coefficient (k) and free carrier density (N) in GaN:Eu$_{TDS}$ samples by measuring the THz pulses that were transmitted through the sample and sapphire substrate. The complex spectra of the transmitted pulses, $E_o(\omega)$, were compared to reference spectra, $E_r(\omega)$ using the relationship,

$$\frac{E_0(\omega)}{E_r(\omega)} \sim 1 + \frac{j\omega d}{c(n_{air} + n_{sub})}\left[-n_{air} + n_{air}n_{sub} + (n + jk)^2 - n_{sub}\right], \tag{4}$$

where d is the GaN:Eu layer thickness, c is the speed of light, n_{air} and n_{sub} are the refractive indexes of the air and sapphire substrate[56]. From this, n and k were obtained at different THz frequencies as shown in Fig. 3e. As example, we find that the index of refraction at 1 THz is ~3.5, while that previously reported for n-type GaN at 1 THz was ~3[57]. This represents a

20% increase in the refractive index due to dilute Eu doping. In addition, the free carrier concentration can be extrapolated from this data and was found to be $N = 6 \times 10^{17}$ cm^{-3}. See Supplementary Note 4 and Supplementary Fig. 6 for more details.

Potential barrier energy in the superlattice structure. The observed bandgap reduction due to Eu doping results in bandgap differences between the undoped and Eu-doped layers within the superlattice structure. This bandgap difference plays an important role in device performance because it can induce potential barriers resulting in a carrier confinement effect similar to that observed in multiple quantum wells (MQWs)[58–61]. Therefore, it must be determined how much of this reduction is due to a change in the conduction band as opposed to the valence band relative to the GaN barrier layers, as this will impact the carrier dynamics differently. Since THz spectroscopy directly probes electrons within the conduction band, we can use the temperature dependence of the THz emission to determine the influence of the potential barriers within the conduction band on the carrier dynamics within the superlattice structures. We performed temperature-dependent THz spectroscopy on the GaN:Eu$_{high}$ and the superlattice samples, as shown in Fig. 4. Here, the peak amplitudes are plotted against temperature (See Supplementary Note 5 and Supplementary Fig. 7 for more details on peak amplitudes determination). Note: The shortest excitation wavelength available was 355 nm, which limited our ability to probe the samples below 200 K[50].

The peak amplitude of the THz emission from the GaN:Eu$_{high}$ sample decreased continuously with increasing temperature within the probe range. On the other hand, the emission from the superlattice first increased between 200 K and 250 K and then decreased continuously at higher temperatures. As described by Eq. (1), the THz emission electric field is proportional to the electron mobility. Consequently, our results suggested that the electron mobility in the GaN:Eu$_{high}$ sample increased continuously with decreasing temperature. The mobility behavior in superlattice structure, however, resembles that observed in GaN/InGaN MQWs and is related to an induced potential barrier for the electrons between the GaN and InGaN layers[62].

To understand this behavior quantitatively, we note that the amplitude of the THz emission in Fig. 4 is proportional to the electron mobility, as described in Eq. (1). We employed a model for the temperature dependence of the electron mobility in bulk GaN to evaluate the mobility in GaN:Eu$_{high}$[63]. In this model, we replace the carrier mobility in GaN with that in Eu-doped GaN, which has been previously measured at room temperature to be $\mu_{Eu}(300) = 53 \mathrm{cm}^2\,\mathrm{V}^{-1}\,\mathrm{s}^{-1}$ [17]. Fitting the data for GaN:Eu$_{high}$ in Fig. 4 to this model yields an expression for the temperature dependence of the carrier mobility in Eu-doped GaN, $\mu_{Eu}(T)$. To evaluate the impact of the superlattice structure on the carrier mobility between the doped and undoped layers and determine the barrier potential for the electrons within this structure, we use $\mu_{Eu}(T)$ in a mobility model that takes into account the barrier height between layers[62,64]. A detailed description of the carrier mobility models is given in the Methods section. After fitting the superlattice structure data in Fig. 4, we obtained a potential barrier value of $\sim 11 \pm 4$ meV for electrons. Given that the growth condition for Eu-doped layer in the superlattice is the same as the condition for GaN:Eu$_{high}$, the bandgap difference between GaN and GaN:Eu layers seems to be ~37 meV, consistent with the difference between ud-GaN and GaN:Eu$_{high}$. Consequently, we can obtain the energy discontinuity on the valence band as ~26 ± 4 meV. This barrier height induces confinement for ~63% of holes at room temperature as determined from the thermal emission, $\exp(-qV_b/k_B T)$, where k_B is the Boltzmann constant, and qV_b represents the barrier height. In addition, this barrier height is low enough as to not impede the hole transport, which can cause poor LED performance as mentioned by Xie et al.[65] Therefore, we suggest that the enhanced Eu luminescence efficiency within the superlattice structure is the result of a small but effective carrier confinement for both electrons and holes, which does not significantly impede their mobility allowing for favorable device performance under current injection.

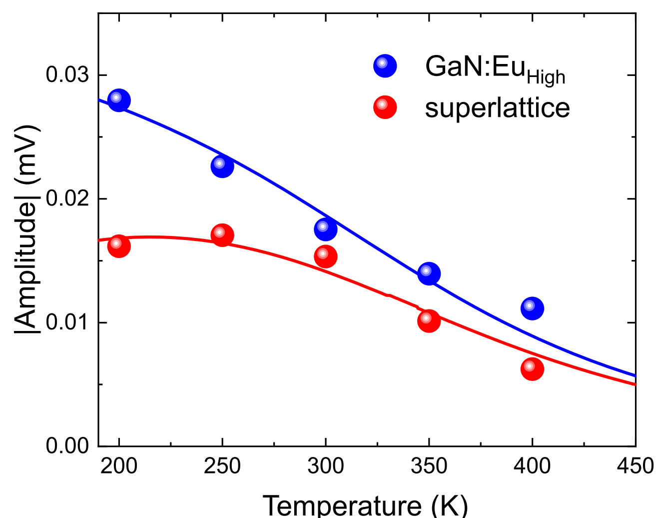

Fig. 4 THz emission peak amplitudes from GaN:Eu$_{high}$ (blue circle) and superlattice (red circle) measured at different temperatures. Blue and red solid lines are fits for GaN:Eu$_{high}$ and superlattice using Eqs. (5) and (7), respectively.

Discussion

The concept of using RE ions to modify the bandgap of a semiconductor host is well-established for certain applications. An example would be the use of RE doping to tune the bandgap of TiO_2, SnO_2, and ZnO nanocrystals to increase photocatalytic activity in the visible range or for wavelength matching in dye-sensitized solar cells[32,33]. Several origins of the bandgap modification have been proposed. A prominent explanation is that the tensile strain that results from the larger ionic radii of the RE ion relative to the atoms they replace leads to a change in the intra-atomic $s-d$ exchange interaction, which is believed to reduce the conduction band edge energy[29–31]. Previous calculations suggest that the introduction of RE ions introduces 4*f* electron states just below the conduction band, which forms a new lowest unoccupied level and modifies the bandgap energy, such as in Nd-doped TiO_2[28]. However, this argument seems to be unsuitable for Eu-doped GaN, where the lowest unoccupied Eu 4*f* levels are much deeper (and not ~40 meV below the CBM)[66–68]. Alternatively, a significant expansion of the lattice in the Eu-doped layers of the superlattice structure has been observed[20]. Since the nature of the bandgap is correlated with the lattice constant[49,69–71], it is expected that even 0.1% doping will result in a decrease in the bandgap due to the lattice expansion in Eu-doped GaN. In addition, increases in the index of refraction have also been reported in a number of dilutely doped RE-doped systems such as Er-doped GaN, and Er-, Sm- or Eu-doped InGaAs, and has been suggested as a simple mechanism to develop optically active waveguide devices[24,36,37,72–75]. The increase in index of refraction and decrease of the bandgap have been computed simultaneously using first-principles methods[68,73]. For example, Maskar *et al.* predicted these behaviors for GaN doped with >6.25% Eu, Sm

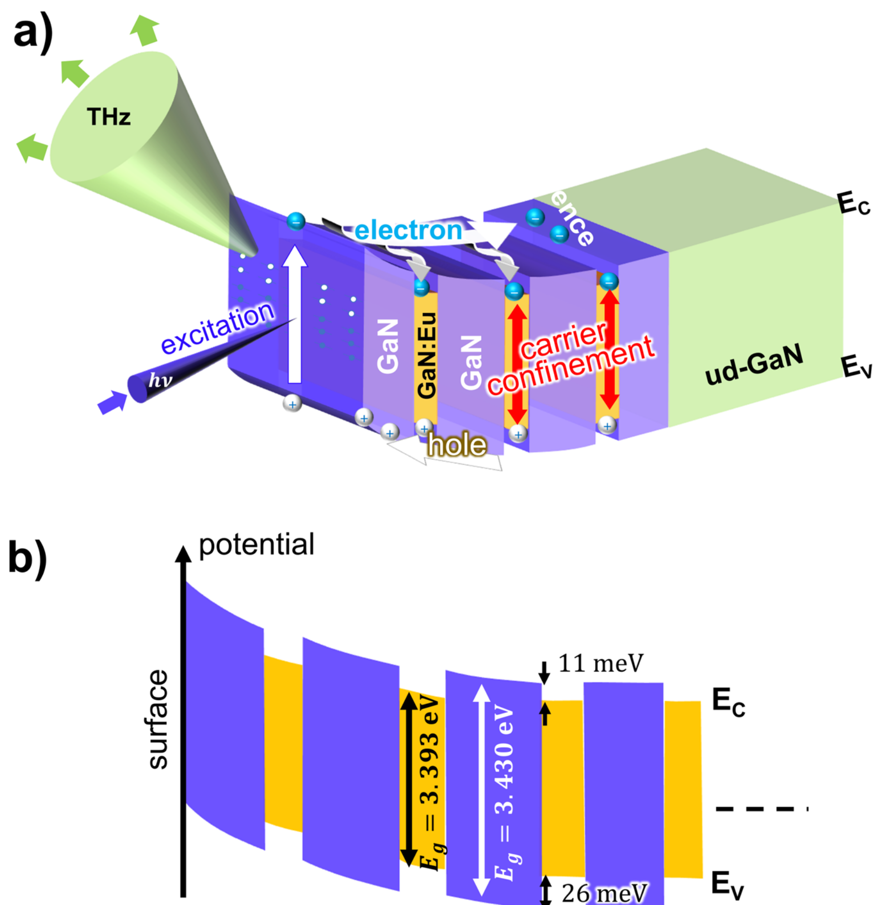

Fig. 5 Schematics of a carrier confinement and band diagram in the superlattice structure. a Schematic of the carrier dynamics and THz emission in the superlattice. Photocarriers are captured into Eu-doped layers due to the bandgap difference between undoped and Eu-doped layers, leading to a higher carrier recombination probability and increased red luminescence. **b** Energy diagram near the surface in superlattice. E_c and E_v represent the energy levels for conduction and valence bands, respectively. Bandgap energies (E_g) for undoped and Eu-doped layers are 3.430 and 3.393 eV, respectively. The potential barriers in the conduction and valence band edge were estimated to be 11 meV and 26 meV, which capture the carriers within Eu-doped layers efficiently without interfering with their transports. Enhanced carrier recombination within the active layers and waveguiding effect due to the refractive index differences between undoped and Eu-doped layers significantly increases the luminescence efficiency in LEDs, as shown in the (**a**) and ref. 16.

and Pm[68]. Experimentally, however, these quantities are not measured or reported simultaneously.

Experimental results that demonstrate a bandgap modification are usually obtained by observing a red-shift in the absorption spectra of the host material, where impurity states and phonon modes can make the analysis complex[27–29,76]. In addition, the primary reason for the RE doping is usually to enhance the properties *of the host*, and not to enhance the emission from the RE ions themselves[28,32,33]. Conversely, the index of refraction is generally determined by fitting the results of reflectivity or ellipsometry measurements, for example in Er-doped GaAs, Er-doped GaN or Er-doped Si[24,36,37,72]. The benefit of using THz measurement techniques to evaluate RE-doped semiconductor systems, as was shown here, is that the bandgap, refractive index, and carrier concentration of RE-doped semiconductors can be determined, as well as barrier potentials for electrons within superlattice structures, using only THz techniques.

Regarding the performance of RE-doped GaN-based optoelectronics devices, the observed bandgap reduction and refractive index increase have significant benefits, particularly when a dilutely doped superlattice structure is implemented. While Er-doped Si superlattice structures have been shown to exhibit a higher performance than bulk Er-doped Si, the underlying principle behind this behavior has not been addressed in detail[21–25]. The results from this work could provide new insight into the origin of the enhancement due to the superlattice structure. In addition, RE doping has been shown to increase the refractive index of host materials experimental approaches in Er-doped GaN[36,37,74,75] or through first-principles calculations[68]. The optical bandgap and index of refraction are related quantities[35], which suggests that RE doping will reduce the bandgap of host semiconductors. In this case, the bandgap reduction in the RE-doped superlattice structure induces the carrier confinement within the active layers, which enhances the carrier recombination and luminescence efficiency[16,60,61]. Additionally, the higher index of refraction will result in a waveguiding effect[37,72,75], increasing the extraction efficiency. These benefits are achieved even at a very low doping concentration of ~0.1%, which also facilitates high crystal-quality growth. Moreover, the reduction of threading dislocations due to the alternating strain between Eu-doped layers and GaN layers was already observed[20]. Taking all of these effects into consideration, it seems that introducing a superlattice structure with dilute Eu doping naturally enhances all of the properties needed to produce high brightness, high-efficiency red GaN LEDs. Critically, we argue that these enhanced optical and electrical properties are not limited to the Eu-doped GaN system. Er-doped GaN, for example, is known to have a higher refractive index than GaN, and GaN/GaN:Er waveguides

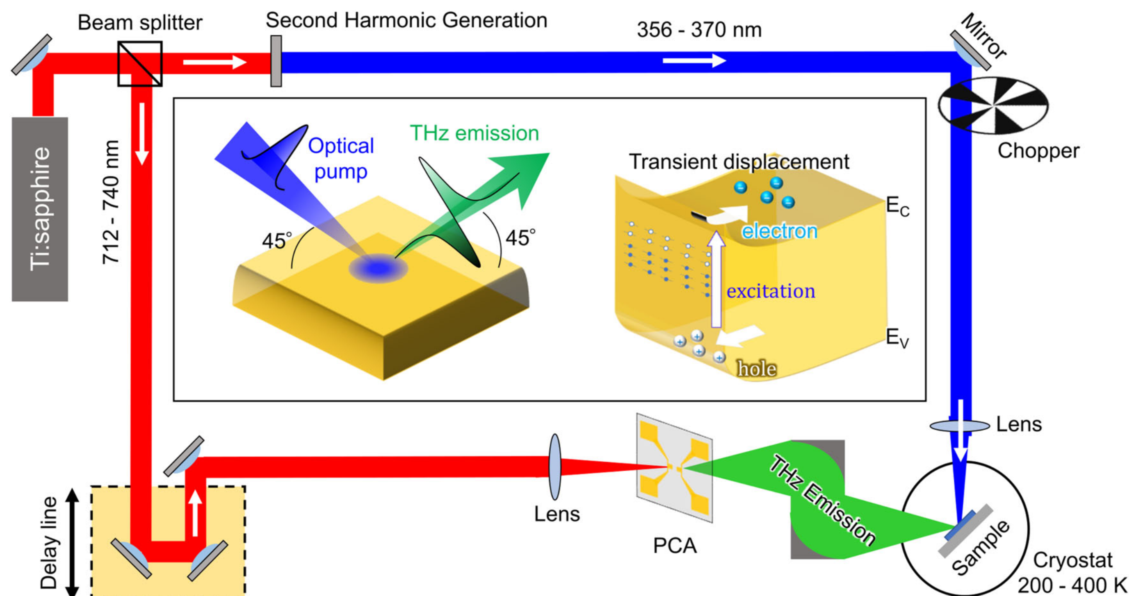

Fig. 6 Diagrams of the TES systems. The system employed a wavelength-tunable fs laser and a cryostat for wavelength and temperature dependent measurements. THz emissions are detected by a photoconductive antenna (PCA). The inset shows the excitation geometry and transient displacement of carriers which generates the THz emission.

and optical amplifiers that take advantage of this have already been reported[36,37,74,75]. By introducing multiple alternating layers, an efficient Er-doped GaN LED operating at the telecom C-band could be achieved.

The use of carrier confinement by introducing a MQW structure is the standard way to increase carrier recombination in commercial LEDs[1–6]. However, although introducing an MQW structure consisting of alternating Eu-doped GaN or Er-doped GaN layers and AlGaN barrier layers was shown to improve the PL intensity and the excitation efficiency of devices[77–81]; the simple superlattice devices have consistently been found to significantly outperform the MQW devices[16,77,78]. One reason could be that the optimal growth conditions of the AlGaN barrier layers needed to form intentional QWs are substantially different from those optimized for the RE-doped GaN layers. Therefore, a sacrifice must be made regarding the quality of either the RE-doped GaN layers or the AlGaN layers. In addition, Xie et al. reported that large potential barriers in MQW structures can interfere with hole transport and cause poor LED performance[65]. For the dilutely doped superlattice structure, the potential barriers for the electrons and holes were found to be <27 meV each, and are therefore not expected to impact carrier transport, while still offering the benefits of carrier confinement. Moreover, the growth conditions between Eu-doped GaN and the GaN layers are close enough, that high crystal quality can be achieved. Figure 5 shows a schematic of the THz and PL emission in a superlattice structure with the determined barrier heights.

Conclusion

Overall, this study confirms that dilute doping of REs into semiconductors produces significant modifications in the optical properties of the host material. By utilizing a superlattice structure, these modified properties naturally produce both carrier confinement and waveguiding effects, thereby enhancing the energy transfer efficiency due to improved carrier recombination, but at a low enough level so as to not impede carrier mobility, as well as increasing the light extraction efficiency. We assert that this is also the origin for the enhanced LED properties previously observed in Er-doped Si superlattice structures, especially given the more recent reports on the increase in the index of refraction and reduction of the bandgap in Er-doped Si. Thus, our findings have answered long-standing questions in the field of RE-based optoelectronic devices as well as helped to unify previous observations and calculations for RE-doped semiconductor systems used for a variety of different applications within numerous fields. Given the universality of bandgap reduction and refractive index increase in a myriad of host semiconductor systems (e.g., GaN, ZnO, TiO_2, SnO_2, GaAs, InGaAs, InP, and Si) with different RE elements (e.g., Eu, Er, Tm, Sm, Gd, Tb), we propose that the superlattice structure should be used as a general approach to enhance the performance of RE-based optoelectronic devices. Furthermore, in the present work, TES is shown as an ideal tool allowing for direct characterization of ultrafast carrier dynamics within RE-doped semiconductors in non-contact/non-destructive manner. Such measurements will be needed to accelerate research on next-generation RE-based optoelectronic devices based on the dilutely doped superlattice structure as TES can yield insight on the bandgap, index of refraction, potential barriers, and carrier density, allowing for a quick and comprehensive analysis.

Methods

Sample fabrication. Bulk undoped GaN (ud-GaN), bulk Eu-doped GaN, and superlattice samples were grown by organo-metallic vapor-phase epitaxy on c-plane sapphire substrates, as shown in Fig. 2. The ud-GaN sample had a 5 µm ud-GaN layer, and one Eu-doped GaN sample had 700 nm thick GaN:Eu layer on a 30 nm low-temperature-grown GaN (LT-GaN) buffer layer, which were named ud-GaN and GaN:Eu_{TDS} (Fig. 2a, b). The other Eu-doped GaN and superlattice samples were initiated with a 30 nm LT-GaN buffer layer followed by a 2 µm ud-GaN layer (Fig. 2c, d). These Eu-doped GaN samples had 300 nm Eu-doped layers followed by 10 nm GaN cap layers. To explore the relationship between Eu doping density and the optical properties, we prepared two GaN:Eu samples with different Eu flow rates, 1.5 slm and 0.5 slm, during GaN:Eu layer growth, which were labeled as GaN:Eu_{high} and GaN:Eu_{low}, respectively. GaN:Eu_{high} is expected to have a doping density of 3-5 $\times 10^{19}$ cm^{-3} [16,19,82,83]. The superlattice sample consisted of 40 pairs of 10-nm-thick GaN

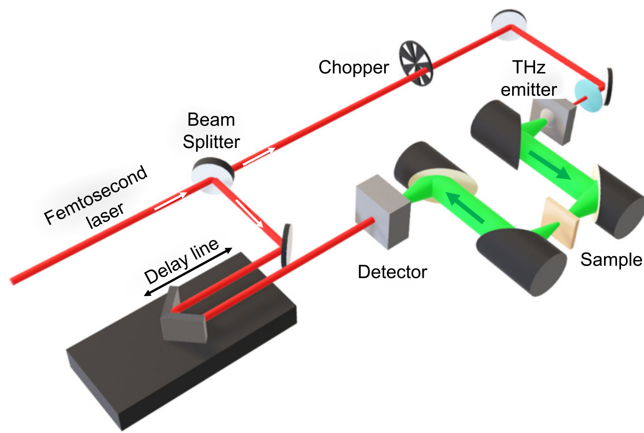

Fig. 7 Experimental configuration of THz time-domain spectroscopy (THz-TDS). Transmission type THz-TDS system (TR-1000; Otsuka Electronics Co. Ltd.) was employed. The measurements were performed at 23 °C and relative humidity of 16%.

layers and 3-nm-thick GaN:Eu layers, which were grown with an Eu flow rate of 1.5 slm. Further details of the sample growth have been reported elsewhere[16,19,82,83].

Optical measurements. THz emission measurements were performed using a TES set-up illustrated in Fig. 6. Femtosecond pulses obtained from a Ti:sapphire laser (center wavelength: 710–740 nm, pulse width: ~100 fs, repetition rate: 80 MHz) were converted into UV pulses through a Beta Barium Borate (BBO) crystal to excite GaN. Samples were excited with a pump power of 6 mW at an incident angle of 45° to obtain the large signal under a phased-array effect[84]. The inset of Fig. 6 shows the geometrical configuration for excitation and emission. The beam spot diameter was approximately 300 µm. Generated THz waves were focused onto a detector by two parabolic mirrors and detected using a dipole-type photoconductive antenna (PCA) fabricated on a low-temperature-grown gallium arsenide. The samples were mounted on a liquid nitrogen cryostat to measure the temperature dependence. Terahertz time-domain spectroscopy (THz-TDS) was used to obtain the free carrier density in GaN:Eu samples. The measurements were performed using a transmission type THz-TDS system (TR-1000; Otsuka Electronics Co. Ltd.) at 23 °C and relative humidity of 16%. Figure 7 shows the experimental configuration. Data were acquired using TR-1000 measurement software (Otsuka Electronics Co. Ltd.).

Determination of barrier heights in the superlattice structure. To describe the relationship between the THz amplitude and the carrier mobility in GaN:Eu$_{high}$, we employed the electron mobility model reported in ref. 63 and replaced the mobility in GaN with that in Eu-doped GaN, μ_{Eu}, as,

$$E_{THz}(T) \propto \mu_{Eu}(T) \propto \mu_{Eu}(300)\frac{B(N)\left(\frac{T}{300}\right)^{\alpha}}{1+B(N)\left(\frac{T}{300}\right)^{\alpha+\beta}}, \quad (5)$$

$$B(N) = \frac{\mu_{min} + \mu_{max}\left(\frac{N_{g,i}}{N}\right)}{\mu_{max} - \mu_{min}}, \quad (6)$$

where α and β are fitting parameters related to the impurity scattering at low temperatures and the lattice scattering at high temperatures, respectively. The values of μ_{min}, μ_{max} and $N_{g,i}$ are estimated from the carrier density dependence of the mobility in bulk GaN, reported in ref. 63, and N is the carrier density. In our calculations, we used $\mu_{Eu}(300) = 53 cm^2\, V^{-1}\, s^{-1}$ for the mobility in Eu-doped GaN as reported in ref. 17. We also used the previously determined free carrier density was for GaN:Eu$_{high}$, $N \sim 6\times 10^{17}\, cm^{-3}$. By fitting the temperature dependent THz amplitudes in Fig. 4 with Eq. (5), we obtained $\alpha \sim -0.2 \pm 0.2, \beta \sim 5.3 \pm 0.2$. The value of α has a large relative error; however, since the contribution of the impurity scattering is significantly less in the measured temperature range, the exact value for α should have a negligible impact on the results[63].

Using these parameters for GaN:Eu$_{high}$, we can now evaluate the impact of the superlattice structure on the carrier mobility between the doped and undoped layers and determine the barrier potential for the electrons within this structure by using a mobility model that takes into account the barrier height, reported in ref. 62. Although this model includes some transport processes, the mobility due to the thermal emission process, μ_{th}, should be dominant in superlattice structure due to the 10 nm thick barrier layers[62]. With these considerations, the THz emission amplitude within the superlattice structure can be described as:

$$E_{THz}(T) \propto \mu_{th}(T) \propto \left(1 + \frac{\mu_{3D}(T)}{qL}\sqrt{8m^*_{3D}qV_b}\right)\exp\left(-\frac{qV_b}{k_B T}\right), \quad (7)$$

where μ_{3D} and m^*_{3D} are the mobility and effective mass of the electrons, q is the elementary charge, L is the sum of GaN and Eu-doped GaN layer thicknesses, k_B is the Boltzmann constant, and qV_b represents the barrier height[62]. Here, we use $\mu_{3D} \sim \mu_{Eu}$ and $m^*_{3D} \sim m^*_{GaN}$: the effective mass of electron in the bulk GaN[64], assuming there is no significant difference between these values in the Eu-doped layer within the superlattice structure and bulk GaN:Eu$_{high}$. It should be noted that the calculated value of qV_b changes by less than 1 meV even when calculated with $2m^*_{GaN}$, justifying this assumption.

Data availability

The data that support the findings of this study are openly available in figshare at https://doi.org/10.6084/m9.figshare.24458992.v1.

Received: 8 July 2023; Accepted: 8 November 2023;
Published online: 20 November 2023

References

1. Li, P., Zhang, X., Qi, L. & Lau, K. M. Full-color micro-display by heterogeneous integration of InGaN blue/green dual-wavelength and AlGaInP red LEDs. *Opt. Express* **30**, 23499–23510 (2022).
2. Hwang, J. L., Hashimoto, R., Saito, S. & Nunoue, S. Development of InGaN-based red LED grown on (0001) polar surface. *Appl. Phys. Express* **7**, 071003 (2014).
3. Chichibu, S., Azuhata, T., Sota, T. & Nakamura, S. Spontaneous emission of localized excitons in InGaN single and multiquantum well structures. *Appl. Phys. Lett.* **69**, 4188–4190 (1998).
4. Baker, T. J., Haskell, B. A., Wu, F., Speck, J. S. & Nakamura, S. Characterization of planar semipolar gallium nitride films on sapphire substrates. *Jpn. J. Appl. Phys.* **45**, L154–L157 (2006).
5. Zhao, H. et al. Growths of staggered InGaN quantum wells light-emitting diodes emitting at 520–525 nm employing graded growth-temperature profile. *Appl. Phys. Lett.* **95**, 061104 (2009).
6. Zhang, S. et al. Efficient emission of InGaN-based light-emitting diodes: toward orange and red. *Photonics Res.* **8**, 1671–1675 (2020).
7. Horng, R.-H. et al. Study on the effect of size on InGaN red micro-LEDs. *Sci. Rep.* **12**, 1324 (2022).
8. Olivier, F., Daami, A., Licitra, C. & Templier, F. Shockley-Read-hall and Auger non-radiative recombination in GaN based LEDs: a size effect study. *Appl. Phys. Lett.* **111**, 022104 (2017).
9. Kou, J. et al. Impact of the surface recombination on InGaN/GaN-based blue micro-light emitting diodes. *Opt. Express* **27**, A643–A653 (2019).

10. Yu, L. et al. Ultra-small size (1–20 μm) blue and green micro-LEDs fabricated by laser direct writing lithography. *Appl. Phys. Lett.* **121**, 042106 (2022).
11. Pandey, A. et al. An ultrahigh efficiency excitonic micro-LED. *Nano Lett.* **23**, 1680–1687 (2023).
12. Zhuang, Z., Iida, D., Velazquez-Rizo, M. & Ohkawa, K. 630-nm red InGaN micro-light-emitting diodes (<20 μm × 20 μm) exceeding 1 mW/mm2 for full-color micro-displays. *Photonics Res.* **9**, 1796–1802 (2021).
13. Li, P. et al. Red InGaN micro-light-emitting diodes (>620 nm) with a peak external quantum efficiency of 4.5% using an epitaxial tunnel junction contact. *Appl. Phys. Lett.* **120**, 121102 (2022).
14. Zhuang, Z., Iida, D. & Ohkawa, K. InGaN-based red light-emitting diodes: from traditional to micro-LEDs. *Jpn. J. Appl. Phys.* **61**, SA0809 (2021).
15. Lin, J. Y. & Jiang, H. X. Development of microLED. *Appl. Phys. Lett.* **116**, 100502 (2020).
16. Mitchell, B., Dierolf, V., Gregorkiewicz, T. & Fujiwara, Y. Perspective: toward efficient GaN-based red light emitting diodes using europium doping. *J. Appl. Phys.* **123**, 160901 (2018).
17. Timmerman, D. et al. Carrier dynamics and excitation of Eu^{3+} ions in GaN. *Phys. Rev. B* **101**, 245306 (2020).
18. Denier Van Der Gon, D. et al. Size dependence of quantum efficiency of red emission from GaN:Eu structures for application in micro-LEDs. *Opt. Lett.* **45**, 3973–3976 (2020).
19. Ichikawa, S. et al. Eu-doped GaN and InGaN monolithically stacked full-color LEDs with a wide color gamut. *Appl. Phys. Express* **14**, 031008 (2021).
20. Mitchell, B. et al. Direct detection of rare earth ion distributions in gallium nitride and its influence on growth morphology. *J. Appl. Phys.* **127**, 013102 (2020).
21. Vinh, N. Q., Przybylińska, H., Krasil'nik, Z. F. & Gregorkiewicz, T. Microscopic structure of Er-related optically active centers in crystalline silicon. *Phys. Rev. Lett.* **90**, 066401 (2003).
22. Kuznetsov, V. P. & Rubtsova, R. A. Special features of the sublimational molecular-beam epitaxy of Si and its potentialities for growing Si:Er/Si structures. *Semiconductors* **34**, 502–509 (2000).
23. Krasilnik, Z. F. et al. Erbium doped silicon single- and multilayer structures for LED and laser applications. *Mater. Res. Soc. Symp. Proc.* **866**, V1.4 (2005).
24. Mula, G., Setzu, S., Manunza, G., Ruffilli, R. & Falqui, A. Optical, electrochemical, and structural properties of Er-doped porous silicon. *J. Phys.Chem. C* **116**, 11256–11260 (2012).
25. Stepikhova, M. V. et al. Properties of optically active Si:Er and $Si_{1-x}Ge_x$ layers grown by the sublimation MBE method. *Thin Solid Films* **369**, 426–430 (2000).
26. Vinh, N. Q., Minissale, S., Vrielinck, H. & Gregorkiewicz, T. Concentration of Er^{3+} ions contributing to 1.5-μm emission in Si/Si:Er nanolayers. *Phys. Rev. B.* **76**, 085339 (2007).
27. Xu, A.-W., Gao, Y. & Liu, H.-Q. The preparation, characterization, and their photocatalytic activities of rare-earth-doped TiO_2 nanoparticles. *J. Catal.* **207**, 151–157 (2002).
28. Li, W. et al. Band gap tailoring of Nd^{3+}-doped TiO_2 nanoparticles. *Appl. Phys. Lett.* **83**, 4143–4145 (2003).
29. Iqbal, J. et al. Raman and highly ultraviolet red-shifted near band-edge properties of LaCe-co-doped ZnO nanoparticles. *Acta Mater.* **57**, 4790–4796 (2009).
30. Kumar, R. & Dosanjh, H. S. A mini-review on rare earth metal doped ZnO nanomaterials for photocatalytic remediation of waste water. *J. Phys. Conf. Ser.* **2267**, 012139 (2022).
31. Apostolova, I., Apostolov, A. & Wesselinowa, J. Band gap tuning in transition metal and rare-earth-ion-doped TiO_2, CeO_2, and SnO_2 nanoparticles. *Nanomaterials* **13**, 145 (2023).
32. Wei, L. et al. Band edge movement in dye sensitized Sm-doped TiO_2 solar cells: a study by variable temperature spectroelectrochemistry. *RSC Adv.* **5**, 70512–70521 (2015).
33. Momeni, M. M. Dye-sensitized solar cells based on Cr-doped TiO_2 nanotube photoanodes. *Rare Metals* **36**, 865–871 (2017).
34. Andreev, B. et al. Realization of photo- and electroluminescent Si:Er structures by the method of sublimation molecular beam epitaxy. *Nanotechnology* **13**, 97 (2002).
35. Ravindra, N. M., Ganapathy, P. & Choi, J. Energy gap-refractive index relations in semiconductors - An overview. *Infrared Phys. Technol.* **50**, 21–29 (2007).
36. Alajlouni, S. et al. Refractive index of erbium doped GaN thin films. *Appl. Phys. Lett.* **105**, 081104 (2014).
37. Smith, T. B. et al. Realization of all-crystalline GaN/Er:GaN/GaN core-cladding optical fiber structures. *Appl. Phys. Lett.* **121**, 192110 (2022).
38. Yang, D. & Tonouchi, M. Understanding terahertz emission properties from a metal–insulator–semiconductor structure upon femtosecond laser illumination. *J. Appl. Phys.* **130**, 055701 (2021).
39. Yang, D., Mannan, A., Murakami, F. & Tonouchi, M. Rapid, noncontact, sensitive, and semiquantitative characterization of buffered hydrogen-fluoride-treated silicon wafer surfaces by terahertz emission spectroscopy. *Light Sci. Appl.* **11**, 334 (2022).
40. Yang, D., Murakami, F., Genchi, S., Tanaka, H. & Tonouchi, M. Noncontact evaluation of the interface potential in VO_2/Si heterojunctions across metal–insulator phase transition. *Appl. Phys. Lett.* **122**, 041601 (2023).
41. Yamahara, K., Mannan, A., Kawayama, I., Nakanishi, H. & Tonouchi, M. Ultrafast spatiotemporal photocarrier dynamics near GaN surfaces studied by terahertz emission spectroscopy. *Sci. Rep.* **10**, 14633 (2020).
42. Jiang, H. et al. Terahertz emission spectroscopy and microscopy on ultrawide bandgap semiconductor β-Ga_2O_3. *Photonics* **7**, 73 (2020).
43. Leitenstorfer, A. et al. The 2023 terahertz science and technology roadmap. *J. Phys. D Appl. Phys.* **56**, 223001 (2023).
44. Sakai, Y., Kawayama, I., Nakanishi, H. & Tonouchi, M. Polarization imaging of imperfect m-plane GaN surfaces. *APL Photonics* **2**, 041304 (2017).
45. Mannan, A. et al. Ultrafast terahertz nanoseismology of GaInN/GaN multiple quantum wells. *Adv. Opt. Mater* **9**, 2100258 (2021).
46. Wais, M. et al. Transition from diffusive to superdiffusive transport in carbon nanotube networks via nematic order control. *Nano Lett.* **23**, 4448–4455 (2023).
47. Murakami, F., Mannan, A., Serita, K., Murakami, H. & Tonouchi, M. Slow optical response of semi-insulating GaN film studied by terahertz emission and photoluminescence spectroscopy. *J. Appl. Phys.* **131**, 185706 (2022).
48. Tonouchi, M. Simplified formulas for the generation of terahertz waves from semiconductor surfaces excited with a femtosecond laser. *J. Appl. Phys.* **127**, 245703 (2020).
49. Shan, W. et al. Dependence of the fundamental band gap of $Al_xGa_{1-x}N$ on alloy composition and pressure. *J. Appl. Phys.* **85**, 8505 (1999).
50. Monemar, B. Fundamental energy gap of GaN from photoluminescence excitation spectra. *Phys. Rev. B* **10**, 676–681 (1974).
51. Braun, C., Mereacre, L., Chen, Z. & Slabon, A. Closing the yellow gap with Eu- and Tb-doped GaN: one luminescent host resulting in three colours. *Sci. Rep.* **12**, 2503 (2022).
52. Nazari, M. & Holtz, M. W. Near-ultraviolet Raman and micro-Raman analysis of electronic materials. *Appl. Phys. Rev.* **5**, 041303 (2018).
53. Reddy, P. et al. The effect of polarity and surface states on the Fermi level at III-nitride surfaces. *J. Appl. Phys.* **116**, 123701 (2014).
54. Grodzicki, M., Moszak, K., Hommel, D. & Bell, G. R. Bistable Fermi level pinning and surface photovoltage in GaN. *Appl. Surf. Sci.* **533**, 147416 (2020).
55. Barker, A. S. & Ilegems, M. Infrared lattice vibrations and free-electron dispersion in GaN. *Phys. Rev. B* **7**, 743 (1973).
56. Neu, J. & Schmuttenmaer, C. A. Tutorial: an introduction to terahertz time domain spectroscopy (THz-TDS). *J. Appl. Phys.* **124**, 231101 (2018).
57. Zhang, W., Azad, A. K. & Grischkowsky, D. Terahertz studies of carrier dynamics and dielectric response of n-type, freestanding epitaxial GaN. *Appl. Phys. Lett.* **82**, 2841–2843 (2003).
58. Dingle, R., Wiegmann, W. & Henry, C. H. Quantum states of confined carriers in very thin $Al_xGa_{1-x}As$-GaAs-$Al_xGa_{1-x}As$ heterostructures. *Phys. Rev. Lett.* **33**, 827 (1974).
59. Göbel, E. O., Jung, H., Kuhl, J. & Ploog, K. Recombination enhancement due to carrier localization in quantum well structures. *Phys. Rev. Lett.* **51**, 1588 (1983).
60. Arif, R. A., Zhao, H., Ee, Y. K. & Tansu, N. Spontaneous emission and characteristics of staggered InGaN quantum-well light-emitting diodes. *IEEE J. Quantum Electron* **44**, 573–580 (2008).
61. Gorai, A. The overlap of electron and hole wavefunctions in the $In_xGa_{1-x}N$/GaN graded quantum well LED is much superior to the symmetrically staggered: even to that of a trapezoidal quantum well. *Optik* **207**, 163829 (2020).
62. Toprasertpong, K., Goodnick, S. M., Nakano, Y. & Sugiyama, M. Effective mobility for sequential carrier transport in multiple quantum well structures. *Phys. Rev. B* **96**, 075441 (2017).
63. Mnatsakanov, T. T. et al. Carrier mobility model for GaN. *Solid State Electron* **47**, 111–115 (2003).
64. Yeo, Y. C., Chong, T. C. & Li, M. F. Electronic band structures and effective-mass parameters of wurtzite GaN and InN. *J. Appl. Phys.* **83**, 1429–1436 (1998).
65. Xie, J. et al. On the efficiency droop in InGaN multiple quantum well blue light emitting diodes and its reduction with p-doped quantum well barriers. *Appl. Phys. Lett.* **93**, 121107 (2008).
66. Hoang, K. Tuning the valence and concentration of europium and luminescence centers in GaN through co-doping and defect association. *Phys. Rev. Mater.* **5**, 034601 (2021).
67. Hoang, K. Rare-earth defects in GaN: a systematic investigation of the lanthanide series. *Phys. Rev. Mater* **6**, 044601 (2022).
68. Maskar, E. et al. Electronic, magnetic, optical and transport properties of wurtzite-GaN doped with rare earth (RE= Pm, Sm, and Eu): First principles approach. *Surf. Interfaces* **24**, 101051 (2021).
69. Wu, J. et al. Temperature dependence of the fundamental band gap of InN. *J. Appl. Phys.* **94**, 4457–4460 (2003).

70. Lo, I. et al. Gate-controlled spin splitting in GaN/AlN quantum wells. *Appl. Phys. Lett.* **88**, 82108 (2006).
71. Lyu, S., Skachkov, D., Kash, K., Blanton, E. W. & Lambrecht, W. R. L. Band gaps, band-offsets, disorder, stability region, and point defects in II-IV-N_2 semiconductors. *Phys. Status Solidi (a)* **216**, 1800875 (2019).
72. Stadler, B. J. H. & Lorenzo, J. P. Increased refractive indices in rare earth doped InP and $In_{0.53}Ga_{0.47}As$ thin films. *Mater. Res. Soc. Symposia Proc.* **422**, 357–362 (1996).
73. Singh, P. & Kumar, R. Investigation of refractive index dispersion parameters of Er doped ZnO thin films by WDD model. *Optik* **246**, 167829 (2021).
74. Ho, V. X. et al. Observation of optical gain in Er-Doped GaN epilayers. *J. Lumin.* **221**, 117090 (2020).
75. Sun, Z. Y. et al. Growth and fabrication of GaN/Er:GaN/GaN core-cladding planar waveguides. *Appl. Phys. Lett.* **114**, 222105 (2019).
76. Reshchikov, M. A. Measurement and analysis of photoluminescence in GaN. *J. Appl. Phys.* **129**, 121101 (2021).
77. Arai, T. et al. Enhanced excitation efficiency of Eu ions in Eu-doped GaN/AlGaN multiple quantum well structures grown by organometallic vapor phase epitaxy. *J. Lumin.* **158**, 70–74 (2015).
78. Mitchell, B. et al. Color-Tunablity in GaN LEDs based on atomic emission manipulation under current injection. *ACS Photonics* **6**, 1153–1161 (2019).
79. Ho, V. X. et al. Room-temperature lasing action in GaN quantum wells in the infrared 1.5 µm region. *ACS Photonics* **5**, 1303–1309 (2018).
80. Al Tahtamouni, T. M., Stachowicz, M., Li, J., Lin, J. Y. & Jiang, H. X. Dramatic enhancement of 1.54 µm emission in Er doped GaN quantum well structures. *Appl. Phys. Lett.* **106**, 121106 (2015).
81. Ben Sedrine, N. et al. Eu-doped AlGaN/GaN superlattice-based diode structure for red lighting: excitation mechanisms and active sites. *ACS Appl. Nano Mater.* **1**, 3845–3858 (2018).
82. Zhu, W. et al. Enhanced photo/electroluminescence properties of Eu-doped GaN through optimization of the growth temperature and Eu related defect environment. *APL Mater.* **4**, 056103 (2016).
83. Mitchell, B. et al. Utilization of native oxygen in Eu(RE)-doped GaN for enabling device compatibility in optoelectronic applications. *Sci. Rep.* **6**, 18808 (2016).
84. Mannan, A. et al. A better understanding of terahertz emission from semiconductor surfaces with a phased-array effect. *AIP Adv.* **11**, 125021 (2021).

Acknowledgements

M.T. acknowledges support in part by JSPS KAKENHI Grant No. JP 23H00184, and JST, CREST Grant Number JPMJCR22O2, Japan. F.M. acknowledges support in part by Grant-in-Aid for JSPS Fellows, JST and Program for Leading Graduate schools: "Interactive Materials Science Cadet Program". F.M. and A.T. acknowledge support in part by the establishment of university fellowships towards the creation of science technology innovation, Grant No. JPMJFS2125. B.M. and V.D. acknowledge support in part by NSF RUI Award No. 2129183. Y.F. acknowledges support in part by JSPS KAKENHI Grant No.JP18H05212, No.JP23H00185 and No.JP23H05449, Japan.

Author contributions

F.M. and B.M. conceived the idea and proposed the research. F.M. performed THz emission measurements. F.M., A.T. and M.T. performed data analyses with support from B.M., V.D. and Y.F. F.M. wrote the original draft of the manuscript, B.T., V.D. and M.T. reviewed and edited, and all authors contributed feedback and comments. M.T. directed and supervised the research.

Competing interests

The authors declare no competing interests.

Ethical approval

Has the research included local researchers throughout the research process – study design, study implementation, data ownership, intellectual property and authorship of publications? It has not included local researchers throughout the research process. Is the research locally relevant and has this been determined in collaboration with local partners? The research is not locally relevant. Please describe whether roles and responsibilities were agreed amongst collaborators ahead of the research and whether any capacity-building plans for local researchers were discussed. The research does not relate to the local researchers. Would this research have been severely restricted or prohibited in the setting of the researchers? If yes, please provide details on specific exceptions granted for this research in agreement with local stakeholders. No. Where appropriate, has the study been approved by a local ethics review committee? If not, please explain the reasons. The research is not locally relevant. Where animal welfare regulations, environmental protection and biorisk-related regulations in the local research setting were insufficient compared to the setting of the researchers, please describe if research was undertaken to the higher standards. The research does not relate to them. Does the research result in stigmatization, incrimination, discrimination or otherwise personal risk to participants? If yes, describe provisions to ensure safety and well- being of participants. No. If research involves health, safety, security or other risk to researchers, describe any risk management plans undertaken. There is no risk. Have any benefit sharing measures been discussed in case biological materials, cultural artefacts or associated traditional knowledge has been transferred out of the country? N/A Please indicate if you have taken local and regional research relevant to your study into account in citations. The research is not locally relevant.

Additional information

Supplementary information The online version contains supplementary material available at https://doi.org/10.1038/s43246-023-00428-6.

Correspondence and requests for materials should be addressed to Masayoshi Tonouchi.

Peer review information *Communications Materials* thanks the anonymous reviewers for their contribution to the peer review of this work. Primary Handling Editors: Klaas-Jan Tielrooij and Aldo Isidori. Peer reviewer reports are available.

Reprints and permission information is available at http://www.nature.com/reprints

Publisher's note Springer Nature remains neutral with regard to jurisdictional claims in published maps and institutional affiliations.

Open Access This article is licensed under a Creative Commons Attribution 4.0 International License, which permits use, sharing, adaptation, distribution and reproduction in any medium or format, as long as you give appropriate credit to the original author(s) and the source, provide a link to the Creative Commons license, and indicate if changes were made. The images or other third party material in this article are included in the article's Creative Commons license, unless indicated otherwise in a credit line to the material. If material is not included in the article's Creative Commons license and your intended use is not permitted by statutory regulation or exceeds the permitted use, you will need to obtain permission directly from the copyright holder. To view a copy of this license, visit http://creativecommons.org/licenses/by/4.0/.

© The Author(s) 2023